

# Moiré-controllable exciton localization and dynamics through spatially-modulated inter- and intralayer excitons in a MoSe<sub>2</sub>/WS<sub>2</sub> heterobilayer

Received: 24 March 2025

Accepted: 29 October 2025

Published online: 11 December 2025

 Check for updatesJiaxuan Guo<sup>1</sup>, Zachary H. Withers<sup>2</sup>, Ziling Li<sup>3</sup>, Bowen Hou<sup>1</sup>, Alexander Adler<sup>2</sup>, Jianwei Ding<sup>2</sup>, Victor Chang Lee<sup>1</sup>, Roland K. Kawakami<sup>3</sup>, Gerd Schönhense<sup>4</sup>, Alice Kunin<sup>5</sup>, Thomas K. Allison<sup>2,6</sup> ✉ & Diana Y. Qiu<sup>1</sup> ✉

Moiré heterobilayers exhibiting spatially varying exciton localization that can be precisely controlled through the twist angle have emerged as exciting platforms for studying complex quantum phenomena. Here, we study the exciton landscape in MoSe<sub>2</sub>/WS<sub>2</sub> heterobilayers through synergistic first-principles GW plus Bethe Salpeter equation (GW-BSE) calculations and complementary time- and angle-resolved photoemission spectroscopy (tr-ARPES). We find that the MoSe<sub>2</sub>/WS<sub>2</sub> heterobilayer has a type I band alignment at large twist angles. In contrast, at small twist angles, there exist simultaneous spatially modulated regions of local type I band alignment, hosting bright intralayer excitons, and local type II band alignment, hosting long-lived interlayer excitons, due to lattice reconstruction in different high-symmetry regions. In tr-ARPES this manifests in the observation of long-lived excitons with electron population in only MoSe<sub>2</sub> at large twist angles, while in samples with small twist angles, signals from two distinct long-lived exciton states with electron population in both layers are observed. Contrary to earlier studies, we find no excitonic hybridization near the low-energy absorption peaks in MoSe<sub>2</sub>/WS<sub>2</sub>, whose splitting can, instead, be explained by the lattice reconstruction.

Two-dimensional transition metal dichalcogenides (TMDs) exhibit remarkable electronic and optical properties, making them exciting platforms for exploring excited-state physics. In monolayer TMDs, the combination of quantum confinement and reduced dielectric screening enhances Coulomb interactions, leading to the existence of strongly-bound excitons, with binding energies of around 0.5 eV, as well as other multiparticle excitations<sup>1–7</sup>. These excitons dominate the linear and nonlinear<sup>8</sup> optical properties of monolayer TMDs and facilitate strong light-matter interactions that enable the

concurrent manipulation of charge, spin, and valley degrees of freedom<sup>9–13</sup>.

When two monolayer TMDs, or other layered 2D materials, with a small lattice mismatch or twist angle are vertically stacked, a moiré pattern that can span several nanometers emerges. This moiré pattern creates a long-range spatially varying potential that can be leveraged to engineer the electronic band structure and explore correlated electron states, such as Mott-insulators<sup>14–19</sup>, Wigner crystals<sup>14,15,17,20–22</sup> and various topological states<sup>23–34</sup>. Often these strongly correlated ground states

<sup>1</sup>Department of Materials Science, Yale University, New Haven, CT, USA. <sup>2</sup>Department of Physics and Astronomy, Stony Brook University, Stony Brook, New York, NY, USA. <sup>3</sup>Department of Physics, The Ohio State University, Columbus, OH, USA. <sup>4</sup>Johannes Gutenberg-Universität, Institut für Physik, Mainz, Germany. <sup>5</sup>Department of Chemistry, Princeton University, Princeton, NJ, USA. <sup>6</sup>Department of Chemistry, Stony Brook University, Stony Brook, NY, USA.

✉ e-mail: [thomas.allison@stonybrook.edu](mailto:thomas.allison@stonybrook.edu); [diana.qiu@yale.edu](mailto:diana.qiu@yale.edu)

are studied via probing excitons<sup>14,17,29,35,36</sup>, necessitating a detailed understanding of the exciton spectra. However, the exciton spectra of heterobilayer samples are complicated and can be difficult to assign correctly. One complication is lattice reconstruction. Unlike in twisted bilayer graphene<sup>37,38</sup>, at small twist angles (large moiré unit cells), TMDs undergo substantial lattice relaxation leading to an atomic reconstruction with strained regions where the stacking is nearly commensurate<sup>39–45</sup>. These strained regions host a large variety of tunable, localized exciton states, including interlayer excitons<sup>46</sup>, inter- and intralayer moiré excitons<sup>47,48</sup>, where the electron and hole sit at different moiré lattice sites, and hybrid states, where inter- and intralayer excitons hybridize<sup>49</sup>. Moreover, the moiré-induced localization enables access to excitons with a distribution of finite momenta, whose spatial confinement has the potential to be exploited as quantum dots and single-photon emitters<sup>50</sup>.

The exciton spectrum of MoSe<sub>2</sub>/WS<sub>2</sub> heterobilayers is particularly complicated. While heterobilayers of MX<sub>2</sub> TMDs (M = Mo, W; X = S, Se) mostly exhibit type II band alignment, in which the conduction band minimum (CBM) and valence band maximum (VBM) lie in different layers<sup>51–54</sup>, MoSe<sub>2</sub>/WS<sub>2</sub> is believed to exhibit near degeneracy of the conduction bands within the two layers. Consequently, the band alignment and the character of excitonic states in MoSe<sub>2</sub>/WS<sub>2</sub> heterobilayers remain the subject of considerable debate. Early first-principles density functional theory (DFT) and many-body GW calculations indicated that MoSe<sub>2</sub>/WS<sub>2</sub> exhibits a type II band alignment, with the VBM in the MoSe<sub>2</sub> layer and the CBM in the WS<sub>2</sub> layer<sup>51–54</sup>. Assumptions about the type II band alignment combined with the apparent near degeneracy of the conduction band in both layers also lead to the hypothesis that three distinct low energy peaks in the optical absorption spectrum arise from the hybridization of interlayer and intralayer exciton states<sup>55</sup>. However, more recent experiments and corresponding model calculations indicate that MoSe<sub>2</sub>/WS<sub>2</sub> actually has a type I band alignment with both the VBM and CBM in the MoSe<sub>2</sub> layer. Experimentally, angle-resolved photoemission spectroscopy (ARPES) measurements incorporating electrostatic doping to populate the conduction band show some evidence for the CBM being in MoSe<sub>2</sub><sup>56</sup>, and reflectance contrast spectra as a function of doping density reveal that charged excitons only form in the MoSe<sub>2</sub> layer in large twist-angle MoSe<sub>2</sub>/WS<sub>2</sub> heterostructures, consistent with a type I band alignment<sup>57,58</sup>. Theoretically, a phenomenological model for intra- and interlayer excitons, fit to the experimental differential reflectance signal of MoSe<sub>2</sub>/WS<sub>2</sub> as a function of the out-of-plane electric field, suggests that the MoSe<sub>2</sub> CBM is lower than the WS<sub>2</sub> CBM by about 50 meV<sup>59</sup>. The hybrid exciton hypothesis<sup>49,55</sup> for the splitting of exciton peaks near the MoSe<sub>2</sub> A resonance has also been challenged, as reflectance spectroscopy and photoluminescence (PL) measurements show no evidence of out-of-plane dipoles near the MoSe<sub>2</sub> A peak<sup>57,59,60</sup>. The controversy over this basic property of a widely-studied TMD heterobilayer highlights the need for synergistic first principles theory that can capture the complex interplay of crystal structure and many-body effects with experimental techniques that can track exciton dynamics in momentum space.

In this work, we employ a combination of first-principles GW and GW plus Bethe Salpeter equation (GW-BSE) calculations and time- and angle-resolved photoemission spectroscopy (tr-ARPES) to investigate the quasiparticle (QP) band alignment of MoSe<sub>2</sub>/WS<sub>2</sub> heterobilayer and the character of the low-energy excitons near the MoSe<sub>2</sub> A resonance. We find that in the absence of atomic reconstruction, consistent with large twist angles (small moiré unit cell), the MoSe<sub>2</sub>/WS<sub>2</sub> heterobilayer exhibits a uniform type I band alignment after many-electron interaction effects are included at the GW level. At small twist angles (large moiré unit cell), there is a large atomic reconstruction resulting in strained high-symmetry stacking regions, where the strain in each layer considerably alters the electronic structure, consistent with studies in other TMD bilayers<sup>43,44</sup>. This large reconstruction results in the

simultaneous emergence of alternating domains of local type I band alignment, hosting bright intralayer excitons, and local type II band alignment, hosting interlayer excitons, in the moiré supercell of MoSe<sub>2</sub>/WS<sub>2</sub>, though the global band alignment remains type I. We compare these calculations to tr-ARPES measurements of the excitons, which measure the momentum distributions of the participating electrons and holes<sup>61–63</sup>, the binding energy of the excitons<sup>64</sup>, and also the layer occupation of the electron via the extreme surface sensitivity of ARPES. In our tr-ARPES measurements, we observe long-lived intralayer excitons, with electron population only in the MoSe<sub>2</sub> layer, for samples with large twist angle, while for samples with small twist angles and large moiré unit cells, we observe both long-lived intra- and interlayer exciton species with different binding energies, consistent with our calculations. Finally, our GW-BSE calculations on moiré-free heterobilayers that are strained to match the moiré-driven reconstruction reveal that contrary to previous hypotheses of the existence of hybrid excitons<sup>49,55</sup>, the lowest-energy excitons in the MoSe<sub>2</sub>/WS<sub>2</sub> heterostructure are purely intralayer excitons, with negligible interlayer character. We note that the strain induced by the lattice reconstruction shifts absorption peaks in different high-symmetry stacking regions, and we determine that the co-existence of the three distinct stacking regions contributes to the formation of the three low-energy exciton peaks seen in the optical spectrum at small twist angles<sup>49,57,59</sup> and the two distinct lowest energy excitons in our tr-ARPES measurements.

## Results

### Band alignment at different twist angles

We start by calculating the absolute band alignment of individual isolated monolayers with respect to the vacuum level<sup>51–54</sup>. Figure 1a, d shows the vacuum-aligned DFT band structure of the individual monolayers using the Perdew-Burke-Ernzerhof (PBE) generalized gradient approximation (GGA)<sup>65</sup>, which exhibits type II band alignment with the valence band in the MoSe<sub>2</sub> layer and the conduction band in the WS<sub>2</sub> layer. Spin-orbit coupling splits the conduction band of WS<sub>2</sub> by 30 meV, and the CBM of MoSe<sub>2</sub> is nearly degenerate with WS<sub>2</sub>, lying only 27 meV above the WS<sub>2</sub> CBM, between the spin-orbit split bands, consistent with previous DFT calculations<sup>52</sup>. However, when we consider many-electron interactions and correct the band energies by the GW approximation, the MoSe<sub>2</sub> CBM becomes lower than the WS<sub>2</sub> CBM by 73 meV resulting in a type I band alignment (Fig. 1b, e). Of course, in a real heterostructure, even if wavefunctions of the individual monolayers do not hybridize at the band edge, the electronic states are still screened by both layers. To isolate the role of bilayer screening on the band alignment, we then perform GW calculations for each monolayer using screening that includes the polarizability of both layers in the random phase approximation (RPA)<sup>66,67</sup>, essentially treating the second layer as a substrate whose only contribution is to the polarizability<sup>3,68–70</sup>. The bilayer screening renormalizes the QP bandgap, reducing the gap in WS<sub>2</sub> from 2.48 eV to 2.22 eV and the gap in MoSe<sub>2</sub> from 2.15 eV to 1.99 eV, but the overall type I GW band alignment remains unchanged (Fig. 1c, f).

In a real heterobilayer, the band alignment may also be influenced by atomic reconstruction<sup>43–45,71,72</sup>. Next, we explore the effect of atomic reconstruction on the band alignment at both large twist angles, where the bandstructure at the GW level can be explicitly calculated, and small twist angles, where we approximate large-area reconstructions as regions of nearly uniform stacking (see the Section IV in Supplemental Material). A detailed discussion of the crossover from large to small twist angles (defined as near 0° or 60°) can be found in the Supplemental Material Section VII. We start by exploring the effect of twist angle on atomic reconstruction by constructing large supercells with a MoSe<sub>2</sub> monolayer stacked on a WS<sub>2</sub> monolayer at 8 different twist angles (1.8°, 11.2°, 19.1°, 27.8°, 35.5°, 43.9°, 51.7°, 60°). Then, we relax the supercells using molecular dynamics (MD) following previous

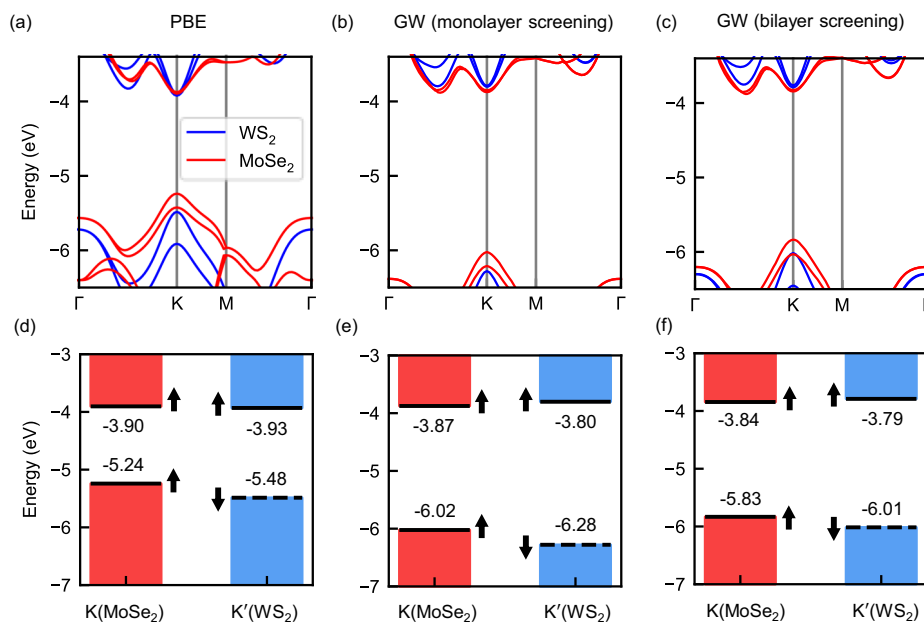


**Fig. 1 | Band structure and alignment of monolayer MoSe<sub>2</sub> and WS<sub>2</sub> across different computational methods.** **a–c** Band structures of monolayer MoSe<sub>2</sub> (red) and WS<sub>2</sub> (blue) calculated by DFT (with the Perdew–Burke–Ernzerhof (PBE) generalized gradient approximation), GW with monolayer and bilayer dielectric screening. Calculations are performed individually for each monolayer, and the bands are shifted so that the vacuum level is set to zero to obtain the band

alignment. The bilayer dielectric screening is obtained from the heterobilayer MoSe<sub>2</sub>/WS<sub>2</sub>. **d–f** Corresponding band alignments of MoSe<sub>2</sub>/WS<sub>2</sub> at the K/K' point. Solid (dashed) lines indicate spin up (down) bands. DFT calculations show a type II band alignment, while one-shot G<sub>0</sub>W<sub>0</sub> calculations (both monolayer and bilayer screening) indicate type I band alignment.

**Table 1 | Molecular dynamics (MD) forcefield relaxation of MoSe<sub>2</sub>/WS<sub>2</sub> moiré supercells at different twist angles**

Angle	Moiré length	Number of atoms	Max. strain (WS <sub>2</sub> )	Max. strain (MoSe <sub>2</sub> )
1.8°	6.1 nm	2112	0.030 Å (1.2%)	0.027 Å (0.8%)
11.2°	2.8 nm	456	0.012 Å (0.4%)	0.012 Å (0.4%)
19.1°	3.5 nm	699	0.007 Å (0.3%)	0.008 Å (0.3%)
27.8°	5.8 nm	1884	0.005 Å (0.2%)	0.005 Å (0.2%)
35.5°	3.3 nm	627	0.005 Å (0.2%)	0.006 Å (0.2%)
43.9°	1.1 nm	75	0.006 Å (0.2%)	0.006 Å (0.2%)
51.7°	6.5 nm	2373	0.011 Å (0.3%)	0.013 Å (0.4%)
60.0°	7.5 nm	3462	0.025 Å (0.8%)	0.030 Å (0.9%)

For the relaxed structure at each twist angle, the moiré length, the number of atoms in the supercell, and the maximum strain amplitude in the relaxed WS<sub>2</sub> layer and MoSe<sub>2</sub> layer are shown.

workflows<sup>44</sup>. The size of the moiré superlattice and the maximum strain due to reconstruction in each layer after relaxation are reported in Table 1. The smallest moiré supercell appears at 43.9° with only 75 atoms and a moiré lattice constant of 1.1 nm. In the small moiré cell, the change in lattice constants due to atomic strain is  $\pm 0.006$  Å, indicating that there is almost no reconstruction. This small amount of strain has a negligible effect on the band energies (see Supplementary Fig. 2 in Supplementary Material). When the twist angle is near 0° or 60°, the moiré supercell is much larger, extending 6–7 nm, and includes thousands of atoms. At these twist angles, there is a large reconstruction. For example, in the case of a 60° twist angle, the lattice constant of the both the MoSe<sub>2</sub> and WS<sub>2</sub> layers experience a maximum strain of 0.9%. At this level of strain, band energies shift by hundreds of milli-electronvolts (see Supplementary Fig. 2 in the Supplemental Material), which is considerably larger than the CBM offset between MoSe<sub>2</sub> and WS<sub>2</sub> in the absence of moiré reconstruction, suggesting the possibility of a twist-angle dependent change in band alignment.

We start by analyzing the small moiré supercell case, for a twist angle of 43.9° where the reconstruction is small. Figure 2a, b shows the crystal structure and corresponding Brillouin Zone (BZ). DFT and GW

calculations are performed directly on the relaxed supercell. Figure 2c shows the DFT band structure colored according to the projected density of states on each layer. The band edges of the MoSe<sub>2</sub> and WS<sub>2</sub> layers are at the  $\gamma$  and  $\kappa$  points of the moiré BZ, respectively, as expected from the unfolding of the moiré BZ shown in Fig. 2b. At the DFT level, MoSe<sub>2</sub>/WS<sub>2</sub> has type II band alignment, which is identical to that of the isolated monolayers. At the GW level (Fig. 2d), the MoSe<sub>2</sub> CBM lies 106 meV below the WS<sub>2</sub> CBM, so the heterostructure has type I band alignment, which is again consistent with calculations on the isolated monolayers. Therefore, at 43.9°, or more generally, at large twist angles when the moiré lattice is small, the moiré potential does not change the band alignment of MoSe<sub>2</sub>/WS<sub>2</sub>, and the heterostructure has a type I band alignment across the entire moiré lattice.

We then investigate the case where the twist angle is near 60°, and the moiré superlattice is large. Figure 3a shows the moiré superlattice. Three distinct stacking regions that form after the relaxation are labeled H<sub>X</sub><sup>M</sup>, denoting a configuration where the central atom is a metal atom stacked on a chalcogen atom in the neighboring layer, H<sub>M</sub><sup>M</sup>, denoting a central metal atom stacked on a metal atom, and H<sub>X</sub><sup>X</sup>, denoting a central chalcogen in one layer stacked with a chalcogen in

the other layer. Figure 3b shows the strain distribution in the same moiré supercell. Positive (negative) percentages mean that the lattice is under compressive (tensile) strain. We see that the MoSe<sub>2</sub> layer is under tensile strain in the H<sub>X</sub><sup>M</sup> region and compressive strain in the H<sub>X</sub><sup>X</sup> region, while WS<sub>2</sub> experiences the opposite strain. In the H<sub>M</sub><sup>M</sup> region both materials are relatively unstrained. Within a radius of 1.2 nm, which roughly corresponds to the radius of the exciton (see

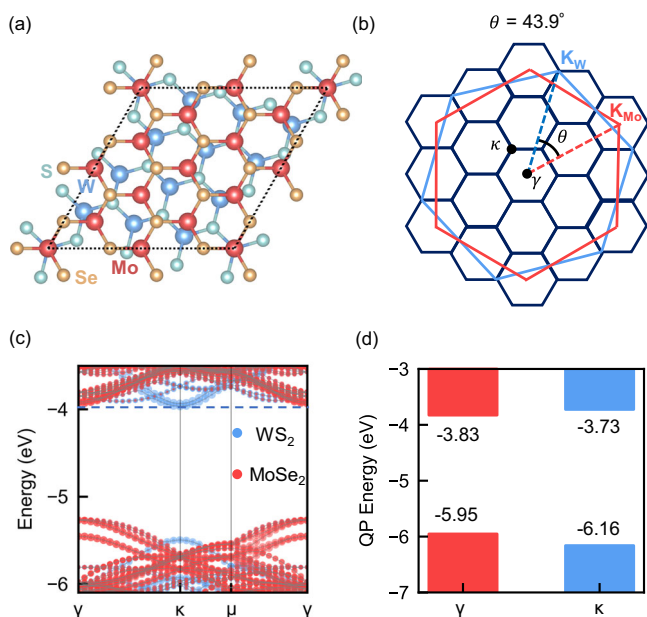


**Fig. 2 | Supercell calculations for the MoSe<sub>2</sub>/WS<sub>2</sub> heterostructure with a 43.9° twist angle.** **a** Atomic structure of 43.9° twist-angle MoSe<sub>2</sub>/WS<sub>2</sub> (top view). **b** Brillouin Zones (BZ) of MoSe<sub>2</sub> (red), WS<sub>2</sub> (blue), and moiré heterostructure (black). The MoSe<sub>2</sub> K point (K<sub>Mo</sub>) is folded to the  $\gamma$  point of the moiré BZ, while the WS<sub>2</sub> K point (K<sub>W</sub>) is folded to the  $\kappa$  point of the moiré BZ. **c** DFT band structure colored according to the projected density of states on each layer. The blue dashed line marks the position of the WS<sub>2</sub> CBM, which is lower than the MoSe<sub>2</sub> CBM by 34 meV, highlighting the type II band alignment at the DFT level. **d** Quasiparticle (QP) band edge at  $\gamma$  and  $\kappa$  of the moiré BZ obtained from GW calculations. The MoSe<sub>2</sub> CBM (red), located at  $\gamma$ , is lower than WS<sub>2</sub> CBM (blue), located at  $\kappa$ , by 102 meV. At the GW level, MoSe<sub>2</sub>/WS<sub>2</sub> has a type I band alignment.

Supplemental Material Section VIII), the standard deviation of the lattice constants in H<sub>X</sub><sup>M</sup>, H<sub>X</sub><sup>X</sup> and H<sub>M</sub><sup>M</sup> are 0.002 Å, 0.005 Å, and 0.006 Å, respectively (see the Section IV in Supplemental Material).

Since the radius of each stacking region for the large moiré superlattice is comparable to the exciton radius<sup>2</sup>, and the strain is relatively uniform within each region, it is reasonable to approximate each region of the moiré superlattice as a heterobilayer with a quasi-uniform strain. We start by determining the change in the band alignment due to the strain in each stacking region at the GW level. Since each stacking is not perfectly commensurate, it is not possible to construct a unit cell with the correct average strain. Instead, to obtain the correct band alignment, we start by calculating the absolute VBM and CBM energies with respect to the vacuum level of monolayer MoSe<sub>2</sub> and WS<sub>2</sub> and incorporate screening taken from the bilayer with the correct stacking configuration. Figure 3c shows the CBM and VBM of MoSe<sub>2</sub> and WS<sub>2</sub> with lattice constants under different strains. Circles indicate unstrained lattice constants in the H<sub>M</sub><sup>M</sup> region. Squares mark the average lattice constant in the H<sub>X</sub><sup>M</sup> and H<sub>X</sub><sup>X</sup> regions. Triangles mark maximum or minimum lattice constants appearing at the boundary of H<sub>X</sub><sup>M</sup> and H<sub>X</sub><sup>X</sup> regions. Our results are consistent with the widely recognized fact that tensile strain decreases both the band gap and the absolute energy of the band edges at the K point in TMDs, whereas compressive strain increases them<sup>73,74</sup>. In the H<sub>X</sub><sup>X</sup> region, MoSe<sub>2</sub> is stretched while WS<sub>2</sub> is compressed, so the MoSe<sub>2</sub> CBM decreases and the WS<sub>2</sub> CBM increases, resulting in local type I band alignment with a band gap of 1.92 eV compared to the bandgap of 1.99 eV found in the unstrained bilayer. The opposite trend is observed in the H<sub>X</sub><sup>M</sup> region, leading to local type II band alignment with a bandgap of 1.86 eV.

Our GW calculations show that MoSe<sub>2</sub>/WS<sub>2</sub> has type I band alignment at large twist angles, where the moiré lattice and reconstruction are small, and both local type I and II band alignment in different high-symmetry regions at small twist angles, where the moiré lattice and reconstruction are large. The coexistence of two types of band alignment introduces the possibility of hosting both intralayer and interlayer excitons in different regions of space within the same heterobilayer.

### Excitons and absorption spectra

Next, we investigate excitons that can arise in these different regions within the *ab initio* GW plus Bethe Salpeter equation (GW-BSE) approach<sup>75,76</sup>. To avoid the computational demand of performing

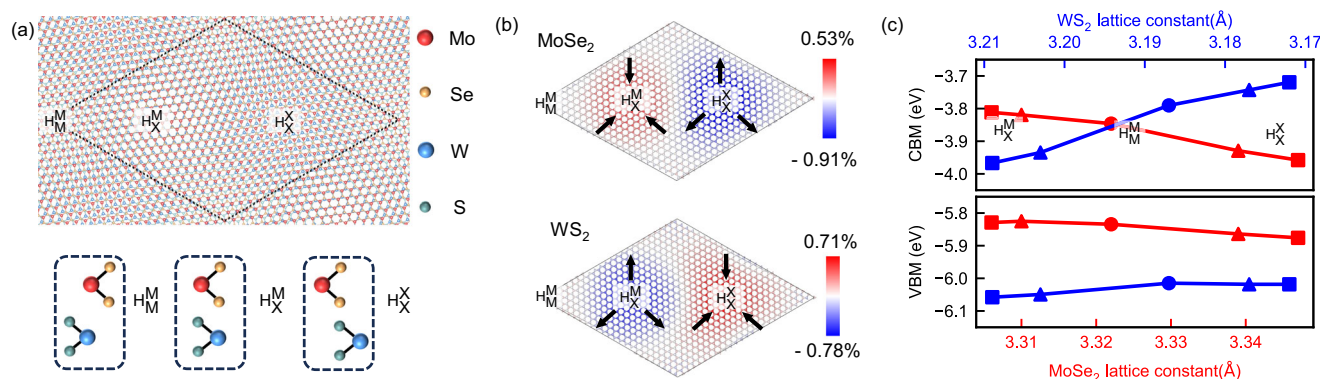


**Fig. 3 | Strain distribution and band alignment in various high-symmetry regions of the MoSe<sub>2</sub>/WS<sub>2</sub> moiré supercell at a 60° twist angle.** **a** Moiré lattice for 60° twist angle MoSe<sub>2</sub>/WS<sub>2</sub> (top). H<sub>X</sub><sup>M</sup>, H<sub>X</sub><sup>X</sup>, and H<sub>M</sub><sup>M</sup> (where M is the transition metal atom and X is the chalcogen atom) are three high-symmetry regions in the unit cell. Their stacking configurations are shown in the black dashed box (bottom). **b** Strain distribution in the same moiré lattice plotted as a variation in local lattice constants from equilibrium. Red (positive) indicates compressive strain; blue (negative) indicates tensile strain. In the H<sub>X</sub><sup>X</sup> region, MoSe<sub>2</sub> is under compressive strain while WS<sub>2</sub> is under tensile strain. The H<sub>X</sub><sup>M</sup> region shows the opposite. **c** GW band edges

(conduction band minimum (CBM) and valence band maximum (VBM)) of strained monolayer MoSe<sub>2</sub> and WS<sub>2</sub> with bilayer screening. All energies are aligned relative to the vacuum level. In each region, WS<sub>2</sub> and MoSe<sub>2</sub> are strained in opposite directions, so MoSe<sub>2</sub> is plotted with increasing strain, and WS<sub>2</sub> is plotted with decreasing strain. Circles are unstrained lattice constant in H<sub>M</sub><sup>M</sup>. Squares are average length of the lattice constants in high-symmetry regions H<sub>X</sub><sup>M</sup> and H<sub>X</sub><sup>X</sup>. Triangles are maximum or minimum length of the lattice constant, appearing at the boundary of regions H<sub>X</sub><sup>M</sup> and H<sub>X</sub><sup>X</sup>. Results indicate type I band alignment in the H<sub>X</sub><sup>X</sup> region and type II band alignment in the H<sub>X</sub><sup>M</sup> region.

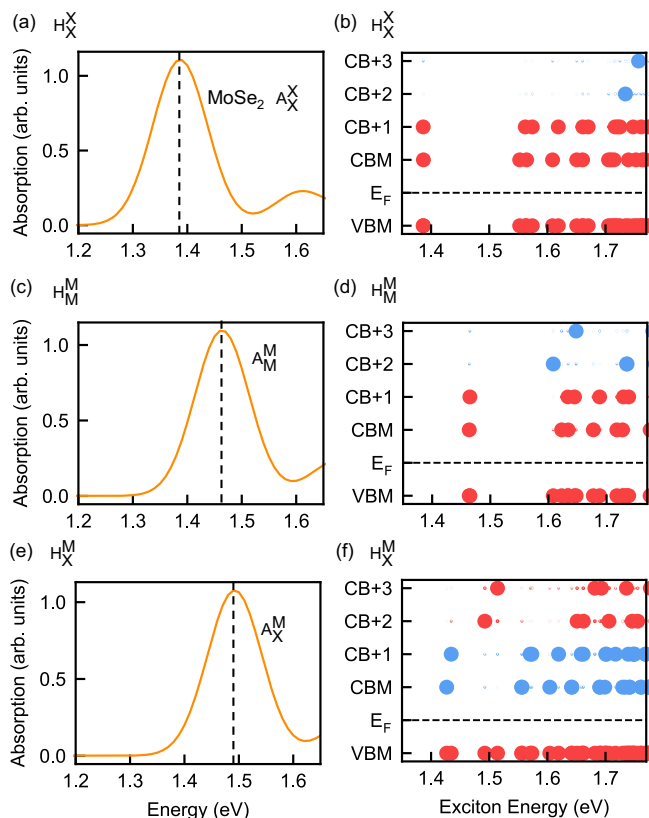


**Fig. 4 | Absorption spectra and excitonic compositions at three distinct high-symmetry regions.** **a, c, e** Absorption spectra of MoSe<sub>2</sub>/WS<sub>2</sub> in different high-symmetry regions with a constant broadening of 0.05 eV. BSE calculations are performed in a patch of 0.193 Å<sup>-1</sup> around the K point in the BZ. The highest peak corresponds to the MoSe<sub>2</sub> A exciton and its center is marked with a black dashed line. The exciton peak position shifts due to different strain in the three high-symmetry regions. **b, d, f** Contributions of different quasiparticle (QP) bands to each exciton state. MoSe<sub>2</sub> valence band maximum (VBM), conduction band minimum (CBM), and higher conduction band (CB+n) contributions are in red, while WS<sub>2</sub> conduction band contributions are in blue. The exciton state can be written as a linear combination of electron-hole pairs  $|S\rangle = \sum_{\nu ck} A_{\nu ck}^S |\nu ck\rangle$ , where  $A_{\nu ck}^S$  is the electron-hole amplitude for the valence band  $\nu$  and conduction band  $c$  at  $k$ -point  $k$ . The size of each dot is proportional to  $\sum_{ck} |A_{\nu ck}^S|^2$  for valence-band states, and  $\sum_{\nu k} |A_{\nu ck}^S|^2$  for conduction-band states. Intralayer and interlayer excitons are clearly distinguishable, indicating that no hybrid excitons contribute to the main peak in the absorption spectrum in each stacking region.

calculations on the full moiré supercell, we again make the reasonable approximation that each stacking region is well-described as a uniform heterobilayer. To account for both interlayer and intralayer excitons, we construct a strained commensurate unit cell of MoSe<sub>2</sub>/WS<sub>2</sub>. Because the commensurate cell has slightly different strain than the high symmetry stacking regions in the reconstructed moiré superlattice, we then treat the change in energy due to strain from the moiré lattice as a first order perturbation on the energies of the commensurate bilayer. This is reasonable since the strain is small and the wavefunctions do not hybridize near the K point.

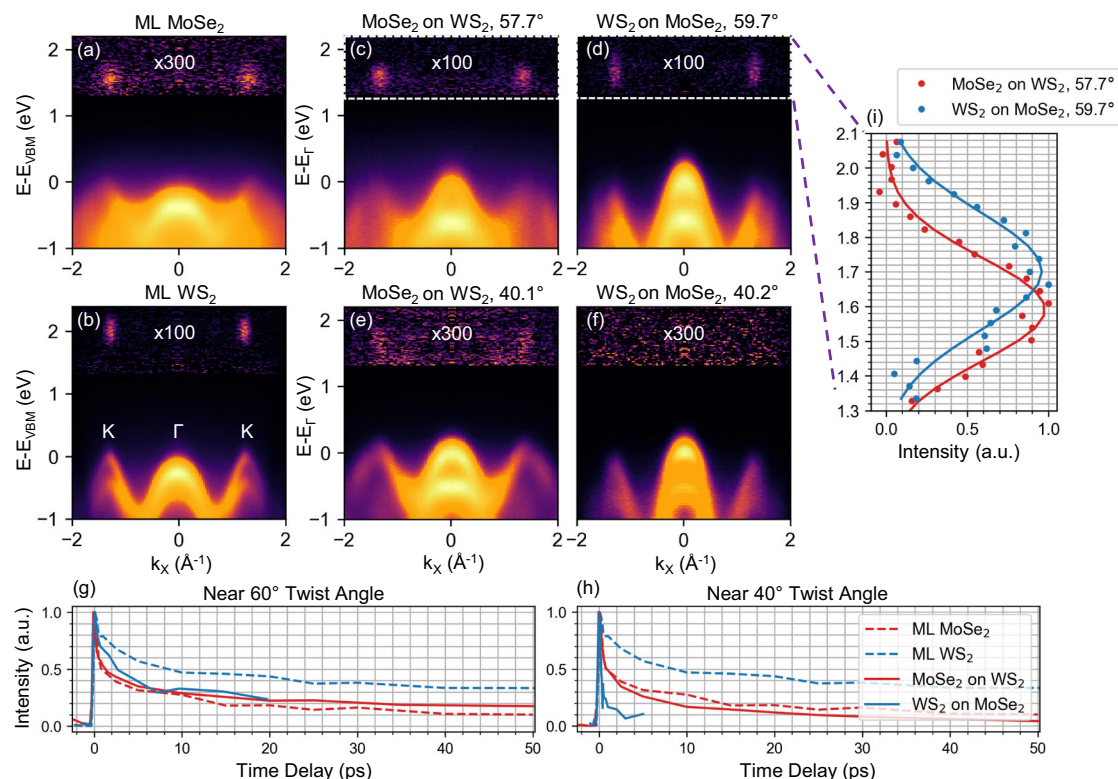
Figure 4a, c, e shows the calculated absorption spectrum corresponding to each high-symmetry stacking region, and (b), (d), and (f) show the contribution of different QP bands projected onto the MoSe<sub>2</sub> or WS<sub>2</sub> layer to the exciton wavefunction at each energy. In the Tamm-Dancoff approximation<sup>76,77</sup>, the exciton can be written as a linear combination of electron-hole pairs  $|S\rangle = \sum_{\nu ck} A_{\nu ck}^S |\nu ck\rangle$ , where  $A_{\nu ck}^S$  denotes the electron-hole amplitude at the  $k$  point in the reciprocal space.  $\nu$  and  $c$  are indices for the valence and conduction bands respectively and  $S$  is the principle quantum number of the exciton. In

Fig. 4b, d, f, every exciton is depicted as a column of points, where the size of each dot corresponds to the square of the electron-hole amplitude,  $\sum_{ck} |A_{\nu ck}^S|^2$  for valence-band states, and  $\sum_{\nu k} |A_{\nu ck}^S|^2$  for conduction-band states.

From this decomposition, the lowest energy exciton appears in the H<sub>X</sub><sup>X</sup> region where the bandgap is smallest. It is a purely intralayer exciton corresponding to the MoSe<sub>2</sub> A exciton. We note that contrary to previous hypotheses<sup>49,55</sup>, the MoSe<sub>2</sub> A exciton does not include any interlayer hybridization and comes purely from the MoSe<sub>2</sub> layer. In our calculations, the GW correction lifts the near degeneracy of the MoSe<sub>2</sub> and WS<sub>2</sub> conduction band edges, which was the basis of previous hypotheses of inter- and intralayer hybridization<sup>55</sup>. However, even when the two conduction bands are nearly degenerate, we still do not see hybrid excitons in our BSE calculation. Some higher energy interlayer excitons (above or near the continuum) do exhibit a degree of hybridization due to interaction with the continuum of lower energy intralayer excitons. (see details in Supplementary Material VI).

Next, we turn to understanding the absorption features in different stacking regions. The absorption spectrum of MoSe<sub>2</sub>/WS<sub>2</sub> with a near 60-degree twist is dominated by three distinct exciton peaks at 1.39 eV, 1.46 eV, and 1.49 eV. As previously noted, the H<sub>X</sub><sup>X</sup> region is dominated by a peak corresponding to the intralayer MoSe<sub>2</sub> A exciton at 1.39 eV, which has a binding energy of 0.53 eV. For convenience, we will refer to this as the A<sub>X</sub><sup>X</sup> exciton. In the H<sub>M</sub><sup>M</sup> region, the band alignment remains type I, and the lowest energy exciton is still the intralayer MoSe<sub>2</sub> A exciton (A<sub>M</sub><sup>M</sup>), now shifted to a higher energy of 1.46 eV. It has a similar binding energy of 0.53 eV. In the H<sub>X</sub><sup>M</sup> region, since there is type II band alignment, the lowest energy exciton is an interlayer exciton (I<sub>X</sub><sup>M</sup>) with the hole in the MoSe<sub>2</sub> layer and the electron in the WS<sub>2</sub> layer. The interlayer exciton is nearly dark, and the absorption spectrum is dominated by the bright intralayer exciton in MoSe<sub>2</sub> (A<sub>X</sub><sup>M</sup>) at 1.49 eV. In the H<sub>X</sub><sup>M</sup> region, the binding energy of the interlayer exciton is 0.43 eV, while the binding energy of the intralayer exciton is 0.53 eV. We note that the experiment is performed on an hBN substrate, which may renormalize the exciton binding energy to 200–300 meV<sup>59</sup>. Accounting for the renormalization may bring the experimental results in closer alignment with theory. Although it is hard to observe the interlayer exciton directly in reflectance contrast experiment because of its weak oscillator strength, it can be brightened by applying out-of-plane electric field. The existence of the interlayer exciton in the H<sub>X</sub><sup>M</sup> region at an energy between A<sub>X</sub><sup>M</sup> and A<sub>X</sub><sup>X</sup> is consistent with experimental observation of a weak dispersion of the second and third absorption peaks under a perpendicular electric field<sup>57,59</sup>. The energy difference between the A<sub>X</sub><sup>M</sup> and A<sub>X</sub><sup>X</sup> peaks is about 100 meV, which is similar to the difference in energy between the first and third absorption peaks observed in previous optical measurements<sup>57,59</sup>. Thus, we attribute the three low-energy peaks in the experimental spectrum to intralayer excitons in the three different high-symmetry regions, consistent with prior phenomenological work based on continuum model without explicit atomic reconstructions<sup>59</sup>. We note that the energy ordering we calculate for small-twist MoSe<sub>2</sub>/WS<sub>2</sub>, with the bright A<sub>X</sub><sup>X</sup> state being the lowest energy exciton, also explains why photoluminescence is not observed from the interlayer excitons in MoSe<sub>2</sub>/WS<sub>2</sub> at zero electrical bias<sup>60</sup>. This energy ordering is atypical for TMD heterostructures, where the long-lived interlayer exciton is usually the lowest energy state, and has an observable PL signature.

It is worth noting that the energy of the middle peak has more uncertainty in the calculation than the other two peaks. The reason is because H<sub>M</sub><sup>M</sup> regions form the boundary between the other two stacking regions. As a result, it is nearly unstrained, but unlike the other stacking regions, the small strain within a single layer is not uniform but has opposite sign depending on whether it is moving toward the H<sub>X</sub><sup>X</sup> or H<sub>X</sub><sup>M</sup> region. Consequently, there is a larger error in the calculated position introduced by the uniform strain approximation. Also, while this calculation does not account for the possibility of intralayer charge transfer



**Fig. 5 | Tr-ARPES of monolayer WS<sub>2</sub> (ML WS<sub>2</sub>), monolayer MoSe<sub>2</sub> (ML MoSe<sub>2</sub>), and twisted heterobilayers. a–f** K-Γ-K slice constructed from tr-ARPES data set by summing all pump/probe delays 5 ps and longer. The signal above 1.3 eV is multiplied by the constant displayed to show the exciton signal within the band gap. A nonlinear color scale is used to make all features visible. Logarithmic and linear scale versions appear in the Supplemental Materials. Normalized intensity traces

comparing the integrated exciton decay of the monolayer samples to hetero-bilayers with (g) small and (h) large relative twist angles. i Energy distribution curves (EDCs) of the exciton signal from the small twist angle bilayers with Gaussian fits. The fitted peak position shifts by  $110 \pm 13$  (statistical error)  $\pm 42$  (systematic error) meV upon permutation of the layer stack ordering.

excitons<sup>71</sup>, it sufficiently captures interlayer and intralayer excitons localized at each moiré site, which are expected to be much brighter in the absorption spectrum than charge transfer excitons.

### TR-ARPES

To experimentally determine the nature of the excitons produced in different heterostructures and also compare dark excitons, we apply tr-ARPES to MoSe<sub>2</sub>/WS<sub>2</sub> samples with different twist angles and different layer stacking orders. For samples with large twist angles, the K valleys of the two layers are easily discernible in momentum-space maps and tr-ARPES directly reports on the layer occupation of the electron component of the exciton wave function after photoexcitation. For samples with small twist angles, where the K valleys of the two layers coincide in momentum space, tr-ARPES can still delineate between inter- and intralayer excitons via the extreme surface sensitivity of the technique. Photoelectron signals from the lower layer are heavily attenuated due to the very small electron mean free path at -20 eV energy<sup>56,78,79</sup>, such that our measurement predominantly measures the electron population in the top-most layer of the heterostructure. The Stony Brook time-resolved ARPES beamline and its application to 2D materials have been described previously<sup>61,80–82</sup>. Heterostructure regions of the samples are selected using an aperture in a real-space image plane of the momentum microscope<sup>83</sup>. The high data rate of the Stony Brook beamline enables us to perform a systematic series of measurements on many samples. In all experiments, the samples are excited with 2.4 eV pump photon energy, which initially populates many exciton states in both layers. In this study, we focus on the long-lived excitons persisting after initial relaxation.

Figure 5a–f shows 2D cuts of the 3D ARPES data along the K-Γ-K direction for 6 different samples, for pump-probe delays greater than

5 ps, recorded with 25.2 eV photon energy. Figure 5a, b show signals from monolayer MoSe<sub>2</sub> and WS<sub>2</sub>, Fig. 5c, d are for heterostructures with twist angles near 60° (the small twist/large moiré supercell condition) and Fig. 5e, f are for heterostructures near 40° (the large twist/small moiré supercell condition). For the monolayers, the energy scale is referenced to the global VBM at K. For the bilayers, the precise maximum at K is not clearly visible due to the photoemission matrix element effect, therefore we reference energies to the local VBM at Γ (E<sub>Γ</sub>). The monolayer signals show the VBM at K, while the hetero-bilayer signals show that the VBM at Γ is nearly degenerate with the MoSe<sub>2</sub> VBM at K, with the WS<sub>2</sub> VBM at K substantially lower in energy, consistent with our calculations and previous work<sup>84</sup>. Similar to previous ARPES work<sup>56</sup> and also consistent with our GW-BSE calculations, in the bilayers we observe a 490–590 meV splitting of the valence bands at Γ due to strong hybridization of the chalcogen p<sub>z</sub> orbitals.

Exciton signals are observed above the VBM but below the CBM due to the exciton binding energy<sup>63,85–89</sup>. Figure 5g, h shows the pump-probe delay dependence of the exciton signals at K for the different samples. Monolayer exciton signals (shown in both Fig. 5g, h) appear at energies consistent with PL measurements<sup>90–92</sup>, and decay on the 10–100 ps timescale, consistent with our previous work<sup>61</sup>. For the bilayers, signals recorded from MoSe<sub>2</sub> on WS<sub>2</sub>, which are sensitive to the electron population in the MoSe<sub>2</sub> layer, show the same dynamics as the intralayer excitons in monolayer MoSe<sub>2</sub> regardless of the twist angle. The exciton signal appears at  $1.59 \pm 0.03$  eV above the E<sub>Γ</sub>, which is in reasonable agreement with the calculated excitation energy of the A<sub>X</sub><sup>X</sup> exciton of 1.39 eV. In contrast, signals recorded from WS<sub>2</sub> on MoSe<sub>2</sub>, which are sensitive to the electron population in the WS<sub>2</sub> layer, show a strong twist-angle dependence. In large-twist WS<sub>2</sub> on MoSe<sub>2</sub> samples, no long-lived signals are observed in ARPES. This suggests that the

long-lived excitons in large-twist-angle samples are intralayer excitons with both the hole and the electron residing in the MoSe<sub>2</sub> layer, consistent with the type I band alignment predicted in our calculations.

However, for samples with near 60° twist angle, we do observe a long-lived electron population in the WS<sub>2</sub> layer, which indicates the presence of long-lived interlayer excitons coexisting with the intralayer excitons. Furthermore, the interlayer excitons appear at a different photoelectron energy. Figure 5i shows the energy distribution curves (EDCs) of the long-lived exciton signal from the near 60° bilayers, along with the Gaussian fits. The signal observed from interlayer excitons in the small-twist-angle WS<sub>2</sub>-on-MoSe<sub>2</sub> sample appears at  $110 \pm 13$  (statistical error)  $\pm 42$  (systematic error) meV higher photoelectron energies than the photoelectron signals from intralayer excitons in the small-twist-angle MoSe<sub>2</sub>-on-WS<sub>2</sub> sample. This energy shift is consistent with the expected signature of an interlayer exciton  $I_X^M$  in the  $H_X^M$  stacking region. The calculated excitation energy of  $I_X^M$  is 40 meV higher than the energy of the  $A_X^X$  exciton. In addition, the valence band edge in the  $H_X^M$  region is 47 meV higher than the  $H_X^X$  region, which means that photoionization of the  $A_X^X$  exciton leaves the hole unrelaxed by 47 meV with a corresponding reduction in the photoelectron energy referenced to the global VBM, leading to an overall energy shift of 87 meV for the tr-ARPES signal of  $I_X^M$  compared to  $A_X^X$ .

## Discussion

In summary, we have performed first-principles GW-BSE calculations on a MoSe<sub>2</sub>/WS<sub>2</sub> heterobilayer and show that the heterobilayer has a type I band alignment when the twist angle is large and the moiré length is small. At small twist angles, when the moiré length is large, we find that the large atomic reconstruction introduces significant strain, resulting in regions of both type I band alignment, hosting bright intralayer excitons, and type II band alignment, hosting long-lived interlayer excitons, at different moiré lattice sites. This spatial modulation between intra- and interlayer excitons could be an interesting platform for exploring novel phases of electrons and charged excitons<sup>93</sup>. Moreover, the system would form a natural lateral heterojunction with the energy landscape directing electron flow to the lower energy region, giving rise to the possibility of enhanced emission and population inversion with long-lived interlayer excitons acting as an exciton reservoir. This work also clarifies the assignment of optical spectra in MoSe<sub>2</sub>/WS<sub>2</sub>. Our BSE calculations show that the absorption spectrum is dominated by three low-energy exciton peaks corresponding to the MoSe<sub>2</sub> A exciton in different stacking regions, with energy splitting in good agreement with experiment<sup>57,59</sup>. We observe no low-energy hybrid excitons, and the absorption peaks appear to be adequately explained by the lattice reconstruction. Our tr-ARPES measurements, which see a long-lived exciton population only in the MoSe<sub>2</sub> layer at large twist angles and at both the energy of the intralayer exciton in MoSe<sub>2</sub> and the interlayer exciton in WS<sub>2</sub> at small twist angles validates our calculations. Our work provides a comprehensive picture of the complex electronic and excitonic landscape in MoSe<sub>2</sub>/WS<sub>2</sub> heterobilayers, where the band alignment and optical properties can be precisely tuned through twist angles. The discovery of coexisting type I and type II band alignments within a single supercell opens pathways for moiré-engineered optoelectronic devices with intrinsic lateral heterojunctions and tunable light-matter interactions.

## Methods

### GW-BSE calculations and molecular dynamics relaxation

We start by performing DFT calculations as implemented in the Quantum ESPRESSO code<sup>94</sup> with the Perdew-Burke-Ernzerhof (PBE) generalized gradient approximation (GGA)<sup>65</sup> for the exchange-correlation energy. Then, we calculate the QP band alignment and exciton states within the GW and GW-BSE formalism on top of the DFT mean field. The GW and GW-BSE calculations, with a fully relativistic

spinor formalism, are performed with the BerkeleyGW package<sup>75,76,95,96</sup>. We construct twisted bilayer TMDs with the help of the TWISTER code<sup>97</sup>, relax atomic structures using the Stillinger–Weber (SW) force field<sup>98</sup> and the parametrized Kolmogorov–Crespi potential<sup>99–101</sup> as implemented in the LAMMPS package<sup>102</sup>, and visualize atomic strain using OVITO<sup>103</sup> and VESTA<sup>104,105</sup>. Additional computational details can be found in the Supplemental Material.

### Sample fabrication and characterization

The WS<sub>2</sub>/MoSe<sub>2</sub>/hBN heterostructures were fabricated using mechanical exfoliation and dry transfer method. First, hexagonal boron nitride (hBN) was mechanically exfoliated onto a highly doped n-type silicon substrate (0.001–0.005 Ω-cm) using Scotch tape. An hBN flake with a thickness of 20–30 nm was selected via optical contrast to construct the heterostructure. Then, monolayer WS<sub>2</sub> and MoSe<sub>2</sub> were mechanically exfoliated onto a polydimethylsiloxane (PDMS) substrate. Second harmonic generation (SHG) spectroscopy was further performed to control the twist angle between the layers. Finally, the monolayer MoSe<sub>2</sub> and WS<sub>2</sub> were sequentially transferred onto the hBN flake using the dry transfer method. Some part of the exfoliated MoSe<sub>2</sub> or WS<sub>2</sub> flake was draped over the edge of the hBN to ensure a conductive pathway exists and sample charging does not occur during ARPES measurements.

The heterostructures with MoSe<sub>2</sub> on WS<sub>2</sub> have twist angles  $57.7^\circ \pm 0.2^\circ$  and  $40.1^\circ \pm 0.3^\circ$ . The photoluminescence and reflection contrast measurements from the monolayer and heterobilayer regions, the SHG characterization of the twist angle, the optical image, and the photoemission electron microscopy (PEEM) image are shown in Supplementary Figs. 7 and 8. The photoluminescence and reflection contrast measurements were acquired at 90 K.

The heterostructures with WS<sub>2</sub> on MoSe<sub>2</sub> have twist angles  $59.7^\circ \pm 0.5^\circ$  and  $40.2^\circ \pm 0.4^\circ$ . The photoluminescence from monolayer and heterobilayer regions, the SHG characterization of the twist angle, the optical image, and the PEEM image are shown in Supplementary Figs. 9 and 10. These measurements were acquired at room temperature.

### Time-resolved ARPES measurements and data analysis

Tr-ARPES measurements were performed at the Stony Brook tr-ARPES beamline facility<sup>61,79–81</sup>. All measurements were done with vacuum pressure at or below  $9 \times 10^{-10}$  torr and were measured with 25.2 eV probe photon energy. All measurements are performed at room temperature and with a pump wavelength of 517 nm (2.4 eV). The monolayer MoSe<sub>2</sub> (ML-MoSe<sub>2</sub>), monolayer WS<sub>2</sub> (ML-WS<sub>2</sub>), and 40° MoSe<sub>2</sub> on WS<sub>2</sub> bilayer were excited with 101 μJ/cm<sup>2</sup> pump fluence. The 58° MoSe<sub>2</sub> on WS<sub>2</sub> bilayer was excited with 193 μJ/cm<sup>2</sup>. The pump pulses were s-polarized during these measurements. The 59° WS<sub>2</sub> on MoSe<sub>2</sub> bilayer was excited with 43 μJ/cm<sup>2</sup> and the 40° WS<sub>2</sub> on MoSe<sub>2</sub> bilayer was excited with 45 μJ/cm<sup>2</sup>. The pump pulses were p-polarized during these measurements. For the bilayer samples, data are collected from a -10 μm region of interest (ROI) selected using a field aperture in a real-space image plane of the microscope<sup>83</sup>.

The data obtained from the instrument is post processed to eliminate image distortions and for image calibration. First, the surface photovoltage (SPV) produced from the pump pulse exciting the Si substrate is corrected for and energy axes referenced to the valence band maxima (VBMs) are generated. The procedure for this correction has been described previously<sup>61,82</sup>. In ML-WS<sub>2</sub>, the VBM is determined by fitting an EDC of the spin-orbit split bands at K with a double Gaussian and using the fitted peak position as the VBM. For ML-MoSe<sub>2</sub>, the ARPES signal at the VBM at K is very weak due to the photoemission matrix element, so the VBM is determined by fitting an EDC from the Γ band with a Gaussian, then adding previously reported 380 meV<sup>106</sup> to determine the true VBM at K. For the bilayer samples, the signal at K is very weak in general so all energies are referenced to the local valence band maximum at Γ,  $E_\Gamma$ . Since the electronic states at Γ have

contributions from both layers, we do not expect the position of  $E_{\Gamma}$  observed in ARPES to depend on the layer orientation. Within the experimental error,  $\Gamma$  and K are energetically degenerate in the bilayer samples.

Once the energy axes are determined, each 3D image ( $k_x, k_y, E$ ) is normalized to the counts within a large ROI around  $\Gamma$ . This normalization accounts for any drift in the photoelectron yield at different pump-probe time delays. A background signal ( $k_x, k_y, E$ ) is constructed from the average of data taken with negative pump-probe time delays and is subtracted from the remaining signal ( $k_x, k_y, E, t$ ).

To produce the time traces shown in Fig. 5g, h, the exciton signal at the K-point is integrated using a  $0.28\text{\AA}^{-1} \times 0.28\text{\AA}^{-1}$   $k_x$ - $k_y$  bin size and an energy bin tuned to capture the entire exciton signal. Then, electron distribution curves (EDCs) are extracted from the same regions of interest in the background-subtracted exciton signal, summing data taken at or after 5 ps pump-probe delay. The EDCs are fit with Gaussians and the extracted peak positions are used for comparison between samples. To produce the K- $\Gamma$ -K cuts, the data is distortion-corrected within the  $k_x$ - $k_y$  plane using thin-spline transformations obtained from symmetry guided image registration<sup>107</sup>. Image shear along the E- $k_x$  and E- $k_y$  axes are corrected using affine transformations. The background subtracted data is stitched to data without background subtraction to show the exciton signal and the valence band signal together. After the shear is eliminated, the data is 6-fold symmetrized in the  $k_x$ - $k_y$  plane. Then, a  $0.10\text{\AA}^{-1}$  bin is used to generate the K- $\Gamma$ -K cut displayed and the exciton signal is multiplied by a constant so that it can be seen. Data taken at and after 5 ps pump-probe time delay is summed to show the final state after the initial dynamics have decayed. Supplementary Figs. 11 and 12 show the K- $\Gamma$ -K cuts on linear and natural logarithmic scales.

The systematic error is dominated by uncertainties in the calibration function that maps time-of-flight in the momentum microscope to energy. Typically features within a spectrum are compared to other features within the same spectrum. Therefore, any systematic offset from the absolute energy would be eliminated when comparing differences within that spectrum. However, here features across different datasets where the systematic errors might differ are compared. Therefore, a cancellation of the systematic error is not expected in this case.

## Data availability

The data used to generate the figures are publicly available in the Materials Data Facility through a <https://doi.org/10.18126/8wvm-ay11>. They can also be obtained from the corresponding authors upon request.

## Code availability

The first-principles calculations are performed with Quantum ESPRESSO<sup>94</sup> and BerkeleyGW<sup>75</sup> software package.

## References

- Wang, G. et al. Colloquium: Excitons in atomically thin transition metal dichalcogenides. *Rev. Mod. Phys.* **90**, 021001 (2018).
- Qiu, D. Y., Da Jornada, F. H. & Louie, S. G. Optical spectrum of MoS<sub>2</sub>: many-body effects and diversity of exciton states. *Phys. Rev. Lett.* **111**, 216805 (2013).
- Ugeda, M. M. et al. Giant bandgap renormalization and excitonic effects in a monolayer transition metal dichalcogenide semiconductor. *Nat. Mater.* **13**, 1091 (2014).
- Qiu, D. Y., Da Jornada, F. H. & Louie, S. G. Screening and many-body effects in two-dimensional crystals: Monolayer MoS<sub>2</sub>. *Phys. Rev. B* **93**, 235435 (2016).
- Chernikov, A. et al. Exciton Binding Energy and Nonhydrogenic Rydberg Series in Monolayer WS<sub>2</sub>. *Phys. Rev. Lett.* **113**, 076802 (2014).
- Mak, K. F. et al. Tightly bound trions in monolayer MoS<sub>2</sub>. *Nat. Mater.* **12**, 207 (2013).
- Ye, Z. et al. Probing excitonic dark states in single-layer tungsten disulphide. *Nature* **513**, 214 (2014).
- Chang Lee, V., Yue, L., Gaarde, M. B., Chan, Y. & Qiu, D. Y. Many-body enhancement of high-harmonic generation in monolayer MoS<sub>2</sub>. *Nat. Commun.* **15**, 6228 (2024).
- Choi, W. et al. Recent development of two-dimensional transition metal dichalcogenides and their applications. *Mater. Today* **20**, 116 (2017).
- Mak, K. F. & Shan, J. Photonics and optoelectronics of 2D semiconductor transition metal dichalcogenides. *Nat. Photonics* **10**, 216 (2016).
- Xiao, D., Liu, G.-B., Feng, W., Xu, X. & Yao, W. Coupled Spin and Valley Physics in Monolayers of MoS<sub>2</sub> and Other Group-VI Dichalcogenides. *Phys. Rev. Lett.* **108**, 196802 (2012).
- Cao, T. et al. Valley-selective circular dichroism of monolayer molybdenum disulphide. *Nat. Commun.* **3**, 887 (2012).
- Mak, K. F., McGill, K. L., Park, J. & McEuen, P. L. The valley Hall effect in MoS<sub>2</sub> transistors. *Science* **344**, 1489 (2014).
- Regan, E. C. et al. Mott and generalized Wigner crystal states in WSe<sub>2</sub>/WS<sub>2</sub> moiré superlattices. *Nature* **579**, 359 (2020).
- Huang, X. et al. Correlated insulating states at fractional fillings of the WS<sub>2</sub>/WSe<sub>2</sub> moiré lattice. *Nat. Phys.* **17**, 715 (2021).
- Ghiotto, A. et al. Quantum criticality in twisted transition metal dichalcogenides. *Nature* **597**, 345 (2021).
- Xu, Y. et al. Correlated insulating states at fractional fillings of moiré superlattices. *Nature* **587**, 214 (2020).
- Li, T. et al. Continuous Mott transition in semiconductor moiré superlattices. *Nature* **597**, 350 (2021).
- Pan, H. & Sarma, S. D. Interaction-driven filling-induced metal-insulator transitions in 2D moiré lattices. *Phys. Rev. Lett.* **127**, 096802 (2021).
- Zhou, Y. et al. Bilayer Wigner crystals in a transition metal dichalcogenide heterostructure. *Nature* **595**, 48 (2021).
- Padhi, B., Chitra, R. & Phillips, P. W. Generalized Wigner crystallization in moiré materials. *Phys. Rev. B* **103**, 125146 (2021).
- Li, H. et al. Imaging two-dimensional generalized Wigner crystals. *Nature* **597**, 650 (2021).
- Wu, F., Lovorn, T. & MacDonald, A. H. Topological exciton bands in moiré heterojunctions. *Phys. Rev. Lett.* **118**, 147401 (2017).
- Wu, F., Lovorn, T., Tutuc, E., Martin, I. & MacDonald, A. H. Topological Insulators in Twisted Transition Metal Dichalcogenide Homobilayers. *Phys. Rev. Lett.* **122**, 086402 (2019).
- Li, T. et al. Quantum anomalous Hall effect from intertwined moiré bands. *Nature* **600**, 641 (2021).
- Devakul, T., Crépel, V., Zhang, Y. & Fu, L. Magic in twisted transition metal dichalcogenide bilayers. *Nat. Commun.* **12**, 6730 (2021).
- Li, H., Kumar, U., Sun, K. & Lin, S.-Z. Spontaneous fractional Chern insulators in transition metal dichalcogenide moiré superlattices. *Phys. Rev. Res.* **3**, L032070 (2021).
- Crépel, V. & Fu, L. Anomalous Hall metal and fractional Chern insulator in twisted transition metal dichalcogenides. *Phys. Rev. B* **107**, L201109 (2023).
- Cai, J. et al. Signatures of fractional quantum anomalous Hall states in twisted MoTe<sub>2</sub>. *Nature* **622**, 63 (2023).
- Tong, Q. et al. Topological mosaics in moiré superlattices of van der Waals heterobilayers. *Nat. Phys.* **13**, 356 (2017).
- Xie, Y.-M., Zhang, C.-P., Hu, J.-X., Mak, K. F. & Law, K. T. Valley-polarized quantum anomalous Hall state in moiré MoTe<sub>2</sub>/WSe<sub>2</sub> heterobilayers. *Phys. Rev. Lett.* **128**, 026402 (2022).
- Su, Y., Li, H., Zhang, C., Sun, K. & Lin, S.-Z. Massive Dirac fermions in moiré superlattices: A route towards topological flat minibands and correlated topological insulators. *Phys. Rev. Res.* **4**, L032024 (2022).

33. Morales-Durán, N. et al. Pressure-enhanced fractional Chern insulators along a magic line in moiré transition metal dichalcogenides. *Phys. Rev. Res.* **5**, L032022 (2023).
34. Wang, C. et al. Fractional Chern insulator in twisted bilayer MoTe<sub>2</sub>. *Phys. Rev. Lett.* **132**, 036501 (2024).
35. Tang, Y. et al. Simulation of Hubbard model physics in WSe<sub>2</sub>/WS<sub>2</sub> moiré superlattices. *Nature* **579**, 353 (2020).
36. Chen, D. et al. Excitonic insulator in a heterojunction moiré superlattice. *Nat. Phys.* **18**, 1171 (2022).
37. Bistritzer, R. & MacDonald, A. H. Moiré bands in twisted double-layer graphene. *Proc. Natl Acad. Sci.* **108**, 12233 (2011).
38. Cao, Y. et al. Unconventional superconductivity in magic-angle graphene superlattices. *Nature* **556**, 43 (2018).
39. Regan, E. C. et al. Emerging exciton physics in transition metal dichalcogenide heterobilayers. *Nat. Rev. Mater.* **7**, 778 (2022).
40. Du, L. et al. Moiré photonics and optoelectronics. *Science* **379**, eadg0014 (2023).
41. Ciarrocchi, A., Tagarelli, F., Avsar, A. & Kis, A. Excitonic devices with van der Waals heterostructures: valleytronics meets twistronics. *Nat. Rev. Mater.* **7**, 449 (2022).
42. Wilson, N. P., Yao, W., Shan, J. & Xu, X. Excitons and emergent quantum phenomena in stacked 2D semiconductors. *Nature* **599**, 383 (2021).
43. Weston, A. et al. Atomic reconstruction in twisted bilayers of transition metal dichalcogenides. *Nat. Nanotechnol.* **15**, 592 (2020).
44. Naik, M. H. & Jain, M. Ultraflatbands and Shear Solitons in Moiré Patterns of Twisted Bilayer Transition Metal Dichalcogenides. *Phys. Rev. Lett.* **121**, 266401 (2018).
45. Li, H. et al. Imaging moiré flat bands in three-dimensional reconstructed WSe<sub>2</sub>/WS<sub>2</sub> superlattices. *Nat. Mater.* **20**, 945 (2021).
46. Rivera, P. et al. Observation of long-lived interlayer excitons in monolayer MoSe<sub>2</sub>-WSe<sub>2</sub> heterostructures. *Nat. Commun.* **6**, 6242 (2015).
47. Tran, K. et al. Evidence for moiré excitons in van der Waals heterostructures. *Nature* **567**, 71 (2019).
48. Jin, C. et al. Observation of moiré excitons in WSe<sub>2</sub>/WS<sub>2</sub> heterostructure superlattices. *Nature* **567**, 76 (2019).
49. Alexeev, E. M. et al. Resonantly hybridized excitons in moiré superlattices in van der Waals heterostructures. *Nature* **567**, 81 (2019).
50. Man, M. K. et al. Experimental measurement of the intrinsic excitonic wave function. *Sci. Adv.* **7**, eabg0192 (2021).
51. Liang, Y., Huang, S., Soklaski, R. & Yang, L. Quasiparticle band-edge energy and band offsets of monolayer of molybdenum and tungsten chalcogenides. *Appl. Phys. Lett.* **103**, 042106 (2013).
52. Kang, J., Tongay, S., Zhou, J., Li, J. & Wu, J. Band offsets and heterostructures of two-dimensional semiconductors. *Appl. Phys. Lett.* **102**, 012111 (2013).
53. Kim, H. & Choi, H. J. Thickness dependence of work function, ionization energy, and electron affinity of Mo and W dichalcogenides from DFT and GW calculations. *Phys. Rev. B* **103**, 085404 (2021).
54. Zhang, C. et al. Systematic study of electronic structure and band alignment of monolayer transition metal dichalcogenides in Van der Waals heterostructures. *2D Mater.* **4**, 015026 (2016).
55. Zhang, L. et al. Twist-angle dependence of moiré excitons in WS<sub>2</sub>/MoSe<sub>2</sub> heterobilayers. *Nat. Commun.* **11**, 5888 (2020).
56. Nguyen, P. *Micro-Focus ARPES of Operating 2D Devices*. PhD Thesis, University of Washington, (2021).
57. Tang, Y. et al. Tuning layer-hybridized moiré excitons by the quantum-confined Stark effect. *Nat. Nanotechnol.* **16**, 52 (2021).
58. Tang, Y. et al. Dielectric catastrophe at the Wigner-Mott transition in a moiré superlattice. *Nat. Commun.* **13**, 4271 (2022).
59. Polovnikov, B. et al. Field-Induced Hybridization of Moiré Excitons in MoSe<sub>2</sub>/WS<sub>2</sub> Heterobilayers. *Phys. Rev. Lett.* **132**, 076902 (2024).
60. Kistner-Morris, J. et al. Electric-field tunable Type-I to Type-II band alignment transition in MoSe<sub>2</sub>/WS<sub>2</sub> heterobilayers. *Nat. Commun.* **15**, 4075 (2024).
61. Kunin, A. et al. Momentum-Resolved Exciton Coupling and Valley Polarization Dynamics in Monolayer WS<sub>2</sub>. *Phys. Rev. Lett.* **130**, 046202 (2023).
62. Karni, O. et al. Structure of the moiré exciton captured by imaging its electron and hole. *Nature* **603**, 247 (2022).
63. Madéo, J. et al. Directly visualizing the momentum-forbidden dark excitons and their dynamics in atomically thin semiconductors. *Science* **370**, 1199 (2020).
64. Boschini, F., Zonno, M. & Damascelli, A. Time-resolved ARPES studies of quantum materials. *Rev. Mod. Phys.* **96**, 015003 (2024).
65. Perdew, J. P., Burke, K. & Ernzerhof, M. Generalized gradient approximation made simple. *Phys. Rev. Lett.* **77**, 3865 (1996).
66. Adler, S. L. Quantum theory of the dielectric constant in real solids. *Phys. Rev.* **126**, 413 (1962).
67. Wiser, N. Dielectric constant with local field effects included. *Phys. Rev.* **129**, 62 (1963).
68. Li, L. et al. Direct observation of the layer-dependent electronic structure in phosphorene. *Nat. Nanotechnol.* **12**, 21 (2017).
69. Qiu, D. Y., da Jornada, F. H. & Louie, S. G. Environmental screening effects in 2D materials: renormalization of the bandgap, electronic structure, and optical spectra of few-layer black phosphorus. *Nano Lett.* **17**, 4706 (2017).
70. Utama, M. I. B. et al. A dielectric-defined lateral heterojunction in a monolayer semiconductor. *Nat. Electron.* **2**, 60 (2019).
71. Naik, M. H. et al. Intralayer charge-transfer moiré excitons in van der Waals superlattices. *Nature* **609**, 52 (2022).
72. Shabani, S. et al. Deep moiré potentials in twisted transition metal dichalcogenide bilayers. *Nat. Phys.* **17**, 720 (2021).
73. Yun, W. S., Han, S., Hong, S. C., Kim, I. G. & Lee, J. Thickness and strain effects on electronic structures of transition metal dichalcogenides: 2H-M X<sub>2</sub> semiconductors (M= Mo, W; X= S, Se, Te). *Phys. Rev. B* **85**, 033305 (2012).
74. Song, W. & Yang, L. Quasiparticle band gaps and optical spectra of strained monolayer transition-metal dichalcogenides. *Phys. Rev. B* **96**, 235441 (2017).
75. Deslippe, J. et al. BerkeleyGW: A massively parallel computer package for the calculation of the quasiparticle and optical properties of materials and nanostructures. *Comput. Phys. Commun.* **183**, 1269 (2012).
76. Rohlffing, M. & Louie, S. G. Electron-hole excitations and optical spectra from first principles. *Phys. Rev. B* **62**, 4927 (2000).
77. A. L. Fetter and J. D. Walecka, *Quantum Theory of Many-Particle Systems* (Courier Corporation, 2012).
78. S. Hüfner, *Photoelectron Spectroscopy: Principles and Applications* (Springer Science & Business Media, 2013).
79. Jones, A. J. et al. Visualizing band structure hybridization and superlattice effects in twisted MoS<sub>2</sub>/WS<sub>2</sub> heterobilayers. *2D Mater.* **9**, 015032 (2021).
80. Corder, C. et al. Ultrafast extreme ultraviolet photoemission without space charge. *Struct. Dyn.* **5**, 054301 (2018).
81. Allison, T. K., Kunin, A. & Schönhense, G. Cavity-enhanced high-order harmonic generation for high-performance time-resolved photoemission experiments. *APL Photonics* **10**, 010906 (2025).
82. Bakalis, J. et al. Momentum-Space Observation of Optically Excited Nonthermal Electrons in Graphene with Persistent Pseudospin Polarization. *Nano Lett.* **24**, 9353 (2024).
83. Schönhense, G., Medjanik, K. & Elmers, H.-J. Space-, time- and spin-resolved photoemission. *J. Electron Spectrosc. Relat. Phenom.* **200**, 94 (2015).

84. Ruiz-Tijerina, D. A. & Fal'ko, V. I. Interlayer hybridization and moiré superlattice minibands for electrons and excitons in hetero-bilayers of transition-metal dichalcogenides. *Phys. Rev. B* **99**, 125424 (2019).
85. Rustagi, A. & Kemper, A. F. Photoemission signature of excitons. *Phys. Rev. B* **97**, 235310 (2018).
86. Perfetto, E., Sangalli, D., Marini, A. & Stefanucci, G. First-principles approach to excitons in time-resolved and angle-resolved photoemission spectra. *Phys. Rev. B* **94**, 245303 (2016).
87. Steinhoff, A. et al. Exciton fission in monolayer transition metal dichalcogenide semiconductors. *Nat. Commun.* **8**, 1166 (2017).
88. Ohnishi, H., Tomita, N. & Nasu, K. Direct determination of exciton wavefunction amplitudes by the momentum-resolved photoelectron emission experiment. *Int. J. Mod. Phys. B* **32**, 1850094 (2018).
89. Chan, Y.-H., Qiu, D. Y., Da Jornada, F. H. & Louie, S. G. Giant self-driven exciton-Floquet signatures in time-resolved photoemission spectroscopy of MoS<sub>2</sub> from time-dependent GW approach. *Proc. Natl Acad. Sci.* **120**, e2301957120 (2023).
90. Wang, G. et al. Polarization and time-resolved photoluminescence spectroscopy of excitons in MoSe<sub>2</sub> monolayers. *Appl. Phys. Lett.* **106**, 112101 (2015).
91. Yuan, L. & Huang, L. Exciton dynamics and annihilation in WS<sub>2</sub> 2D semiconductors. *Nanoscale* **7**, 7402 (2015).
92. Xu, H. et al. Control of Hybrid Exciton Lifetime in MoSe<sub>2</sub>/WS<sub>2</sub> Moiré Heterostructures. *Adv. Sci.* **11**, 2403127 (2024).
93. Dai, D. D. & Fu, L. Strong-coupling phases of trions and excitons in electron-hole bilayers at commensurate densities. *Phys. Rev. Lett.* **132**, 196202 (2024).
94. Giannozzi, P. et al. QUANTUM ESPRESSO: a modular and open-source software project for quantum simulations of materials. *J. Phys. Condens. Matter* **21**, 395502 (2009).
95. Barker, B. A. et al. Spinor GW/Bethe-Salpeter calculations in BerkeleyGW: Implementation, symmetries, benchmarking, and performance. *Phys. Rev. B* **106**, 115127 (2022).
96. Hybertsen, M. S. & Louie, S. G. Electron correlation in semiconductors and insulators: Band gaps and quasiparticle energies. *Phys. Rev. B* **34**, 5390 (1986).
97. Naik, S., Naik, M. H., Maity, I. & Jain, M. Twister: Construction and structural relaxation of commensurate moiré superlattices. *Comput. Phys. Commun.* **271**, 108184 (2022).
98. Stillinger, F. H. & Weber, T. A. Computer simulation of local order in condensed phases of silicon. *Phys. Rev. B* **31**, 5262 (1985).
99. Naik, M. H., Maity, I., Maiti, P. K. & Jain, M. Kolmogorov-Crespi Potential For Multilayer Transition-Metal Dichalcogenides: Capturing Structural Transformations in Moiré Superlattices. *J. Phys. Chem. C* **123**, 9770 (2019).
100. Kolmogorov, A. N. & Crespi, V. H. Smoothest bearings: interlayer sliding in multiwalled carbon nanotubes. *Phys. Rev. Lett.* **85**, 4727 (2000).
101. Kolmogorov, A. N. & Crespi, V. H. Registry-dependent interlayer potential for graphitic systems. *Phys. Rev. B* **71**, 235415 (2005).
102. Thompson, A. P. et al. LAMMPS—a flexible simulation tool for particle-based materials modeling at the atomic, meso, and continuum scales. *Comput. Phys. Commun.* **271**, 108171 (2022).
103. Stukowski, A. Visualization and analysis of atomistic simulation data with OVITO—the Open Visualization Tool. *Model. Simul. Mater. Sci. Eng.* **18**, 015012 (2010).
104. Momma, K. & Izumi, F. VESTA 3 for three-dimensional visualization of crystal, volumetric and morphology data. *J. Appl. Crystallogr.* **44**, 1272 (2011).
105. Momma, K. & Izumi, F. VESTA: a three-dimensional visualization system for electronic and structural analysis. *J. Appl. Crystallogr.* **41**, 653 (2008).
106. Zhang, Y. et al. Direct observation of the transition from indirect to direct bandgap in atomically thin epitaxial MoSe<sub>2</sub>. *Nat. Nanotechnol.* **9**, 111 (2014).
107. Xian, R. P., Rettig, L. & Ernstorfer, R. Symmetry-guided non-rigid registration: The case for distortion correction in multi-dimensional photoemission spectroscopy. *Ultramicroscopy* **202**, 133 (2019).

## Acknowledgements

This work was primarily supported by the U.S. Department of Energy, Office of Science, Basic Energy Sciences under Early Career Award No. DE-SC0021965, which supported theory and first principles calculations on moiré heterostructures (J.G., B.H., V.C.L., D.Y.Q.). Methods to accelerate GW-BSE calculations of heterostructures (J.G., D.Y.Q.) were supported by the NSF under Grant DMR-2114081. Development of the BerkeleyGW code was supported by Center for Computational Study of Excited-State Phenomena in Energy Materials (C2SEP) at the Lawrence Berkeley National Laboratory, funded by the U.S. Department of Energy, Office of Science, Basic Energy Sciences, Materials Sciences and Engineering Division, under Contract No. DE-AC02-05CH11231. This research used resources of the National Energy Research Scientific Computing Center (NERSC), a Department of Energy User Facility operated under contract no. DE-AC02-05CH11231 under award BES-ERCAP-0031507 and BES-ERCAP-0027380, and the Texas Advanced Computing Center (TACC) at The University of Texas at Austin. TR-ARPES work was supported by the U.S. Department of Energy, Office of Science, Office of Basic Energy Sciences under award number DE-SC0022004 and the Air Force Office of Scientific Research under FA9550-20-1-0259. Z.H.W. acknowledges support from the U.S. National Science Foundation Graduate Research Fellowship Program. Fabrication of the samples (Z.L. and R.K.K.) was supported by the U.S. Department of Energy, Office of Science, Basic Energy Sciences under Award No. DE-SC0016379 and the AFOSR/MURI project 2DMagic under Award No. FA9550-19-1-0390.

## Author contributions

D.Y.Q. and T.K.A. conceived the project. J.G., B.H., V.C.L., and D.Y.Q. performed the GW-BSE calculations. Z.H.W., A.A., J.D., A.K., G.S., and T.K.A. carried out tr-ARPES measurements and analysis. Z.L. and R.K.K. fabricated van der Waals heterostructures and performed optical measurements. J.G., Z.H.W., T.K.A., and D.Y.Q. wrote the paper and all authors contributed to the revision of the manuscript.

## Competing interests

The authors declare no competing interests.

## Additional information

**Supplementary information** The online version contains supplementary material available at <https://doi.org/10.1038/s41467-025-66127-7>.

**Correspondence** and requests for materials should be addressed to Thomas K. Allison or Diana Y. Qiu.

**Peer review information** *Nature Communications* thanks the anonymous, reviewer(s) for their contribution to the peer review of this work. A peer review file is available.

**Reprints and permissions information** is available at <http://www.nature.com/reprints>

**Publisher's note** Springer Nature remains neutral with regard to jurisdictional claims in published maps and institutional affiliations.

**Open Access** This article is licensed under a Creative Commons Attribution-NonCommercial-NoDerivatives 4.0 International License, which permits any non-commercial use, sharing, distribution and reproduction in any medium or format, as long as you give appropriate credit to the original author(s) and the source, provide a link to the Creative Commons licence, and indicate if you modified the licensed material. You do not have permission under this licence to share adapted material derived from this article or parts of it. The images or other third party material in this article are included in the article's Creative Commons licence, unless indicated otherwise in a credit line to the material. If material is not included in the article's Creative Commons licence and your intended use is not permitted by statutory regulation or exceeds the permitted use, you will need to obtain permission directly from the copyright holder. To view a copy of this licence, visit <http://creativecommons.org/licenses/by-nc-nd/4.0/>.

© The Author(s) 2025